Highlights

ACORDE: A new application for estimating the dose absorbed by passengers and crews in commercial flights

Hernán Asorey, Mauricio Suárez-Durán, Rafael Mayo-García

- Cosmic rays induced radiation at flight level could be considerably high when including geomagnetic disturbances near the poles.
- Altitude, atmospheric conditions and the geomagnetic field, and their changes should be considered for a more precise calculation of the dose onboard the airplane.
- ACORDE allows the estimation of onboard radiation doses during flights along the real path of the flight anywhere in the World and under real atmospheric and geomagnetic conditions occurred during the flight.

ACORDE: A new application for estimating the dose absorbed by passengers and crews in commercial flights

Hernán Asorey[a,b,*], Mauricio Suárez-Durán[c,1], Rafael Mayo-García[e]

[a]*Medical Physics Department, CNEA, Centro Atomico Bariloche, Av. E. Bustillo 9500, San Carlos de Bariloche, 8400, Rio Negro, Argentina*
[b]*Instituto de Tecnologias en Deteccion y Astroparticulas, CNEA/CONICET/UNSAM, Centro Atomico Constituyentes, Av. Gral. Paz 1499, Villa Maipu, 1650, Buenos Aires, Argentina*
[c]*Universite Libre de Bruxelles (ULB), Boulevard du Triomphe 155, Ixelles, 1050, Brussels, Belgium*
[d]*Universidad de Pamplona, Km 1 Via Bucaramanga Ciudad Universitaria, Pamplona, 1050, Norte de Santander, Colombia*
[e]*Centro de Investigaciones Energeticas Medioambientales y Tecnologicas (CIEMAT), Av. Complutense 40, Madrid, 28040, Madrid, Spain*

Abstract

Atmospheric radiation is mainly produced during the interaction of high energy cosmic rays with the atmosphere. After the first interaction of these primary cosmic rays, a series of radiative and decay processes generate a collective process known as Extensive Air Shower (EAS), with up to 10 secondary particles per primary per GeV at the altitude of the maximum development. As this process occurs for each impinging primary, the integrated flux of secondary particles at typical flight altitudes could easily reach up to 10^6 photons and charged secondary particles with energies in the range of some keV and above per square meter per second. This flux of secondary particles constitutes a risk factor by radiation exposure for the crew members, passengers, and avionics during flights. Moreover, as the dominant, low energy primary flux ($< 20\,\text{GeV}$) is modulated by the heliospheric and geomagnetic conditions, the total radiation dose could be drastically increased during transient heliospheric or geomagnetic disturbances near-to-polar flights. Since the 00's decade, some computational methods have been implemented

*Corresponding author:
Email address: `hernanasorey@cnea.gob.ar` (Rafael Mayo-García)

to estimate the integrated dose along commercial flights. The main advantage of these methods is their short computing time, as they determine the dose from pre-calculated representative libraries based on different analysis in specific situations, and then interpolate and extrapolate atmospheric conditions along a route following a predefined or theoretical track. In this work, we present a new computational method to estimate the dose during a commercial flight by integrating several Monte Carlo-based codes and running them in current high-performance and cloud-based computing facilities. In our method, the expected flux of the secondary radiation is calculated along segments of the real track of commercial flights, obtained from public flight tracker databases. For this, we also consider real-time local atmospheric conditions at each point (extracted from the GDAS database) and correct the total measured flux of primary cosmic rays by the modulation originated by real-time geomagnetic conditions and possible space weather related disturbances. Then, the obtained modulated flux of secondaries at each site of the track is propagated through a Geant4 model of the plane and a human phantom to calculate the total integrated dose. ACORDE (*Application COde for the Radiation Dose Estimation*) is our automatised framework that provides the corresponding effective dose calculation for commercial flights along with the corresponding calculations taking into account all of the aforementioned phenomena. A systematic study over more than 300 commercial flights that occurred in 2021-2022 is also shown compared with the corresponding values obtained from the current calculation methods, where a good agreement is observed for short to intermediate flights ($< 4\,\mathrm{h}$) but a statistically significant deviation to larger doses is observed by the ACORDE calculation for long flights. For the sake of verification with potential future experimental onboard measurements, we provide as examples the result that ACORDE provides estimating the effective dose expected on current radiation counters used in commercial aviation, i.e., gamma-scouts and others, only measuring alpha, beta, gamma, and x-ray radiation. Our results shows that ACORDE can be easily scalable to be used as a complementary tool for the current dose approximation methods.

Keywords: cosmic rays, onboard dose calculation, commercial flights

1. Introduction

Aircraft crews are considered within the highest exposure annual effective dose [?], as commercial flights take place at altitudes over 10 km a.s.l., which results into a much larger exposure to environmental ionizing radiation than at ground level. This radiation, usually known as atmospheric radiation, is produced by the interaction between cosmic rays and the nucleus of the molecules composing the Earth's atmosphere. Studies show that continues exposure to the these radiation can increase the risk factor of radiation-sickness, as is the case with crew members and passengers [?], and radiation damage in the electronics onboard the aircraft (avionics) [?]. Since the 90's, several projects and initiatives have been carried out tending to measure and estimate the effective dose that a person will receive during different type of flights due to the atmospheric radiation [? ?], as for example, the measurement of onboard radiation by using silicon planar detectors finding lower limits for the dose rates values in the range $1.4 - 3.2\,\mu\mathrm{Sv\,h^{-1}}$ [?]. These kind of works engage several governments to revise their national radiation protection laws by the 00's decade pointing to consider the increased atmospheric radiation at flight altitude as occupational risks, as it is clearly stated by ?]. By 2004, different reports from working groups brought together comparative analysis between different calculation codes and specific measurement campaigns, aiming to provide datasets for assessing individual doses and the validity of different approaches [?], and motivating the publication of revised safety standards including the exposure to natural sources of ionising radiation as occupational exposure [?].

As it will be detailed in the next section, at flight altitudes the dose received due to the atmospheric radiation could reach rates of up to $5\,\mathrm{mSv\,h^{-1}}$, attributed to photons and electrons ($\sim$ 30%), protons ($\sim$ 25%), muons ($\sim$ 5%), and neutrons ($\gtrsim$ 40%) [? ?]. Given the impact of neutrons for the dose calculation, several specific measurements of the neutron flux at flight altitudes have been conducted. In particular, ?] installed track etch detectors with a boron foil converter covering different European and transatlantic routes in northern geographical latitudes from 21° to 58° in secular conditions of the geomagnetic field and obtained average ambient equivalent dose rates ($\dot{H}^*(10)$ due to neutrons of $\dot{H}^*(10) = 5.9\,\mu\mathrm{Sv\,h^{-1}}$, while commercial electronic dosimeters gave average values of $\dot{H}^*(10) = 1.4\,\mu\mathrm{Sv}$ during the same flights. Typically, onboard measurement of the non electromagnetic components exceed the capacities of standard radiation detectors extensively used in the industry, such as the Gamma-Scout [?] detectors, that are only sensitive to the electromagnetic and alpha radiation. Moreover, due the impact that the atmospheric and geomagnetic conditions have on the atmospheric radiation [? 1], it might require to deploy sensitive detectors on many routes covering many hours of data registering. This last requirement is due to the dependency of the atmosphere with the geographical position, the effect of the Earth's magnetic field (EMF) [?], and the long-term the solar activity variation associated with the solar cycle [?], with important economic impacts in some particular cases [?]. More recently, ?] carried out the REFLECT (REsearch FLight of EURADOS and CRREAT) research camping by installing more than 20 different type of new and commonly used radiation detectors and dosimeters placed onboard in an small aircraft during a single flight that started and ended at the Vaclav Havel Airport in Prague, and flew during 90 minutes at an altitude of $39,000$ ft (flight level FL390). One of the main conclusions from the REFLECT study is that conventional neutron detectors tends to underestimate the dose as they are not sensitive to high-energy neutrons. Moreover, they also conclude that additional characterization would be required on some commonly used instruments, as they were specifically designed to measure only part of the components of the atmospheric radiation and were not primarily intended for their use in a very complex mixed radiation field and with much wider energy ranges such as the observed in the atmospheric radiation at flight altitudes [?].

Therefore, for now the exposure to ionizing radiation in a flight-by-flight basis can only be estimated by using physical models trying to reproduce the evolution of the interaction between the cosmic rays and the atmosphere under different conditions. Different approaches have been used for this tasks. On the one hand, some tools are based on different cosmic rays and extensive air showers semi-analytical models, i.e., models that use pre-calculated libraries, interpolate and/or extrapolate atmospheric conditions along a predefined and theoretical route, and finally several types of corrections, such as those associated with space weather phenomena, can be applied to obtain the expected dose onboard the aircraft. The Nowcast of Atmospheric Ionizing Radiation for Aviation Safety (NAIRAS) model [? ?] and the well known and extensively used CARI7/CARI7-A codes [?] are good examples of those. Then, the usage of pre-compiled libraries largely reduces the computing times, but can not cover all the complexities associated with the physics mechanisms involved.

Monte Carlo based codes, on the other hand, require much larger computing resources, but are able to properly handle larger complexity levels. Early attempts, such as the original work by [?], calculated the expected flux of atmospheric radiation Ξ under secular and a discrete set of solar modulation parameters at flight altitudes, by using an own designed code based on FLUKA [2]. The main part of these codes tries to calculate the development of the so called Extensive Air Shower (EAS), a cascade of different types of secondary particles that are produced when a cosmic rays interact with the atmosphere via radiative and decay processes that propagate towards the ground following approximately the CR direction [3]. Hence, the atmospheric radiation is the complete population of surviving secondary particles that were produced during interaction of the integrated cosmic ray flux with the air and that are present at a given altitude. Another important part of the Monte Carlo codes are devoted to the calculation of shielding produced by the building materials of the aircraft and the consequent energy that the secondaries deposit over different type of tissues.

During the last decades, the enhancement of computational power and the improvement of new tools to model EAS, such as CORSIKA [? ?], and the interaction of radiation with matter, e.g., Geant4 [?], offer very precise calculation of atmospheric radiation as a function of the altitude under different geomagnetic [1] and atmospheric conditions [4?], which requires considerable computational capabilities. Likewise, current facilities as cloud-based and high performance computing infrastructures open the door to increasing the precision in the dose calculation along commercial flights [?]. In this paper, we show the integration of the former enhancements in an automatised framework called ACORDE (Application COde for the Radiation Dose Estimation). In section 2, we introduce the details of how the flux of cosmic rays is calculated along real commercial flight routes, i.e., for a given set of geographical positions and taking into account the atmospheric conditions and the geomagnetic field. It also presents how is it possible to obtain a precise estimation of the cosmic radiation for each geographical position having used a realistic atmospheric profile at each position. Within this section, a realistic model of the airplane fuselage and a human phantom are also described as well as how ACORDE determines the total effective dose along the route from the secondary flux of particles. Then, in section 3, a systematic study of the integrated effective dose calculated with ACORDE in more than 300 flights that have taken place during 2021 and 2022, and a comparison with the doses obtained by using current available methods is also included. With the aim of easing a quality check of the new ACORDE methodology and precision, results of the effective dose with and without the hadronic and muoninc components of the EAS are also presented for some selected flights. In these calculi, the expected values of radiation that commercial radiation counters would provide are shown, showing that there is a significant increase in the effective dose if all the radiative components would be actually estimated, as ACORDE does. Finally, in section 4 the main conclusions of this work and the future perspectives in the development of ACORDE are presented.

2. Methods

2.1. Modeling of Extensive Air Showers

Cosmic rays (CRs) are defined as particles and atomic nuclei coming from outside the Earth which cover a range of energies from a few GeVs up to $> 10^{20}$ eV [5]. Once these cosmic rays reached the top of the atmosphere ($\sim$ 100 km a.s.l.), their interaction with the elements there presented produced an EAS, as Rossi and Auger discovered in the 1930's [6].

The development and properties of an EAS depend on the energy (E_p) and composition (i.e., gamma, proton, iron, etc.) of the CR which produced it and could reach a maximum production of up to 10^{10} particles at the highest energies. The point at which this maximum takes place is named $X_{\max}$ and it is measured in atmospheric depth X, typically expressed in units of g cm^{-2} [7]. The distribution of secondaries density is well described by the Nishimura-Kamata-Greisen (NKG) lateral distribution function (LDF) in terms of the distance r from the EAS axis, i.e., the direction pointed by the initial momentum of the CR [8].

There are two types of EAS that are defined by the nature of the initial CR: Electromagnetic (EM) showers and hadron-initiated showers. The former are initiated by photons or electrons and most of the processes are mediated by QED interactions, involving mainly two interaction channels: (i) $e^{\pm}$ Bremsstrahlung and (ii) $e^{\pm}$ pair production, and both channels are coupled: photons produced by (i) turn up in the $e^{\pm}$ pair produced by (ii). Thus, new EM secondaries are produced with lower energy E_s, which means that the rate of radiative processes decrease as a function of the atmospheric depth X, i.e., $\langle E_s(X)\rangle = E_p/N(X)$, with N as the total number of secondaries, drops below a critical energy E_c and the ionization losses start to dominate over the radiative losses. When this E_c is reached, the $X_{\max}$ is getting ($\propto \log(E_p)$) with a total number of particles $N_{\max} \propto E_p$, and from this point on the number of particles $N(X)$ starts to monotonically decrease due to: (i) radiative processes are strongly suppressed for $\langle E(X) \rangle < E_c$; and (ii) the atmospheric absorption raises as the air density increases at lower altitudes.

The hadron-initiated EAS produces hadrons and mesons via fragmentation and hadronization of the resulting fragments. The mesons, typically $\pi^{\pm}$ and π^0, have an important impact on the development of these showers due to their lifetime and decay products. For instance, the dominant decay mode of the π^0 is into two photons, which means the production of a new EM shower and the transfer of energy into the EM channel. On the other hand, charged pions propagate through the atmosphere down to altitudes between $4 - 6\,\mathrm{km}$, due to their relative long lifetime $\tau_{\pi^{\pm}} = 2.6 \times 10^{-8}\,\mathrm{s}$ [9]. At these altitudes, the decay into charged muons $\mu^{\pm}$ starts generating the muonic component of the cascade. In this way, the EAS continues its development, with more energy transferring to the EM and μ channels, and once the ground is reached $85 - 90\%$ of E_p is at the EM channel, with a number of particles ratios of $10^2 : 1 : 10^{-2}$ for the EM, muon, and hadronic channels respectively [10].

The hadronic component is located in a region near the shower axis and it is dominated by neutrons and protons. This feature is due to the reduced transference of traverse momentum originated in the characteristic leading particle effect of hadronic interactions, see e.g. [11, 10, 12]. In particular, the neutrons are the only quasi-stable neutral hadrons present in the cascade[1], no ionization or radiative process affect their propagation in the atmosphere, and are produced by spallation processes of protons on ^{14}N and other nuclei in the atmosphere [13, 14]. The energy distribution of these atmospheric neutrons shows a structure produced by energy losses in the atmosphere: a single peak is observed for $E_n \simeq 100\,\mathrm{MeV}$, which is called the quasi-elastic peak; a complex structure for $0.1 \lesssim E_n 10\,\mathrm{MeV}$, caused by several resonances cross-sections depending on the target nuclei; and at lower energies, the distribution follows the power law E_n^{-1}. This means that the measurement of these features depends on parameters as the geographical position and altitude, the current condition of the geomagnetic field, the Solar activity, and the absolute humidity [15]. Even more, at flight altitudes the hadronic

[1]It is possible to consider neutrons as quasi-stable particles since their lifetime is several orders of magnitude larger than the characteristic time of the cascade evolution.

component will not be fully developed and so the contribution of the hadronic component at these altitudes will be much more relevant than at ground level.

EAS simulation is a computational demanding task not only because of the physical interactions to be modelled but also of the large number of particles that are tracked, up to $\sim 10^{10}$ at the higher values of E_p. Several tools are available to perform this type of simulation, but CORSIKA [?] is the most widespread and validated, and it is in continuously upgrading [?]. In specific, this software simulates the EAS produced by a single CR by setting parameters such as the atmospheric model, the local components of the geomagnetic field, and the altitude of the observation level, among others. This means that calculating the expected background radiation at any geographical position and time by using CORSIKA, requires an external tool that sets the aforementioned parameters in a dynamic way. This latest because the local atmospheric profile changes along the year and the flux of CRs is affected by the Solar activity, which in turn affects the geomagnetic field.

The Latin American Giant Observatory (LAGO) [16] has designed and developed ARTI [?] a public accessible toolkit that automates not only the calculation and analysis of the background radiation, but also the estimation of the response of its detectors to this type of radiation [17]. LAGO is a cosmic radiation observatory using water Cherenkov detectors (WCD) installed at 10 different Latin American countries[2], covering a wide range of altitudes and geomagnetic rigidity cutoffs [18]. With the measurement of this radiation along the continent and with the help of ARTI, LAGO is capable to embrace basic research in Astro-particle physics, Space Weather, and Atmospheric Radiation at ground level [19, 1, 20]. ARTI allows the estimation of the expected cosmic radiation at any geographical position under realistic and time-evolving atmospheric and geomagnetic conditions, integrating and articulating CORSIKA,Magneto-Cosmics [?] and Geant4 [?], including its own analysis package [1]. ARTI results have been contrasted and verified through different experiments and measurements at different astroparticle observatories, as most of them take advantage of the atmospheric muon background for the detector calibration [19, 21, 22, 23, 24]. In the latest years, ARTI has been used in a variety of different applications: to characterize new sites at high altitudes for the detection of steady gamma

[2]see the full LAGO sites at http://lagoproject.net

sources or astrophysical transients [20]; to measure space weather phenomena like Forbush decrease by using water Cherenkov detectors [19, 18?]; to estimate the flux of atmospheric muons at underground laboratories [? 25]; to study the distribution of matter at the inner of Latin America volcanoes and its possibles hazards [26, 27, 28, 29]; and, to explore the uses of cosmic radiation to detect improvised explosive devise at warfare fields in Colombia [30]. Taken advantages of its capabilities, in previous works we have used ARTI to understand how space weather phenomena affects the response of water Cherenkov detectors to neutrons produced in EAS [31] and to design new safeguard neutron detector for traffic identification of fissile materials [32, 33].

To calculate the expected flux Ξ of the atmospheric radiation at any geographical position requires of long integration times in order to avoid statistical fluctuations [19?]. This is because a single EAS involves the interaction and tracking of billions of particles during the shower development along the atmosphere, but the atmospheric radiation is caused by the interaction of up to billions of CR impinging the Earth each second. For the modeling of EAS, not only the interactions involved but also the corresponding atmospheric profile at each location that also varies as a function of time should be considered, as it also determines the evolution of the shower [?]. For this reason ARTI is able to handle different atmospheric available models: the MODTRAN model that sets a general atmospheric profile depending on the seasonal characteristics on large areas of the world (say, tropical, subtropical, arctic, and antarctic) [34]; the Linsley's layers model, which uses atmospheric profiles obtained from measurements at predefined sites [35], or the set up of real-time atmospheric profile by using data from the Global Data Assimilation[3] System (GDAS) [36] and characterise them by using the Linsley's model; and finally, an averaged atmospheric profile obtained from the temporal averaging the atmospheric GDAS profiles to build up an averaged density profile at each location for a certain period of time, e.g. one month [4?]. Finally, Ξ is also affected by the variable conditions of the heliosphere and the EMF, as both affect the CR transport up to the atmosphere. As developed and described by Asorey et al. [1], ARTI also incorporates modules to consider changes over the secular magnitude of the EMF and

[3] Data assimilation is the adjustment of the parameters of any specific atmospheric model to the real state of the atmosphere, measured by meteorological observations.

disturbances due to transient solar phenomena, like Forbush decreases or high-energy solar energetic particle (SEP) [?].

Once the primary spectra, the atmospheric profile, and the secular and possible disturbances of the EMF are set, it is possible to obtain Ξ by calculating and injecting in the top of the atmosphere the integrated flux of primaries with energies in the range $Z \times \min(\mathcal{R} < E/\mathrm{eV} < 10^{15}$, where $\mathcal{R}$ is the local directional rigidity cutoff tensor at this place and Z is the charge of the injected primary from protons to irons, $1 \leqslant Z \leqslant 26$, that are expected during the integration time τ and in an area of typically $1\,\mathrm{m}^2$. The complete evolution of each resulting EAS is followed down to the lowest possible kinetic energy of the secondary particles in CORSIKA[4]. Once the atmospheric simulations end, all of those secondaries produced by geomagnetically forbidden primaries are removed by comparing the magnetic rigidity of the parent primary with the time evolution of the local directional rigidity cutoff tensor $\mathcal{R}$. The reader is referred to Asorey et al. [1] for a complete and detailed explanation of all these steps.

As mentioned in section 1, all these processes at this level of detail require of large computing capacity. As an example, to estimate the flux Ξ of the expected secondary particles per square metre per day for a high-latitude site it is required to compute the development of $\sim 10^9$ EAS, and producing a similar number of secondaries at ground level. For this reason, as explained in ?], ARTI is prepared for running on both high performance computing (HPC) clusters and Docker containers executed on virtualised cloud-based environments, such as the European Open Science Cloud (EOSC), and is capable to store and access the produced data catalogues at federated cloud storage servers.

In the next subsection we will show how it is possible to take advantage of all the capabilities of ARTI to perform a precise estimation of the cosmic radiation expected along the real track of a commercial route.

2.2. ACORDE

In view of all the above described functionalities, as it is stated in ?], by using ARTI we are able to precisely calculate the expected flux of atmospheric radiation at any place in the World and under real-time atmospheric

[4]Currently, for CORSIKA v7.7402 compiled with GHEISHA for the low energy interaction models [?], these values are $E_\mathrm{h} = 50\,\mathrm{MeV}$ for hadrons (except neutral pions π^0), $E_\mu = 10\,\mathrm{MeV}$ for muons, and $E_{e^\pm} = E_{\gamma,\pi^0} = 50\,\mathrm{keV}$ for electrons, photons and π^0 [?].

and geomagnetic conditions, and at any altitude above the Earth's surface. As described in subsection 2.1, ARTI has been extensively used and tested in a large variety of astroparticle experiments and technological applications. Based on these experiences and the good agreement observed between the calculated flux of radiation and the different experiments performed to validate this simulation framework, we extended ARTI functionalities to develop ACORDE (*Application COde for the Radiation Dose Estimation*), a framework allowing the automatic and unsupervised calculation of the expected integrated dose that a person will receive during a commercial flight along the plane track. The main difference of ACORDE when compared with existing methods to determine onboard doses, is that ACORDE performs dedicated and intensive Montecarlo simulations of the interaction of radiation with matter to determine, on a flight-by-flight basis, a realistic estimation of the secondary radiation expected at each selected point of the flight track; and the interaction of this secondary radiation with different human tissues to get the corresponding doses. For these reasons, ACORDE is specifically designed to take advantage of running on high performance computing (HPC) clusters operating with SLURM [**?**] or other commonly used workload managers, and in Docker [**?**] containers running on virtualised public or federated cloud-based environments such as the Amazon Web Services (AWS) or the European Open Scientific Cloud (EOSC) [**?**].

The ACORDE workflow is divided into four consecutive steps:

1. obtaining and segmenting the flight track along its route;
2. extracting the atmospheric profile and determining the geomagnetic conditions for each track segment;
3. simulating the secondary flux of particles in the observed conditions of each track; and
4. simulating the shielding effect of the aircraft fuselage and the corresponding effective dose over an anthropomorphic phantom model, and/or a radiation detector on board the plane.

In the industry, each commercial flight is unambiguously identified by an alphanumeric code commonly known as flight number, flight code, or flight designator, which consists of a two-character airline designator followed by a 1 to 4 digit number. ACORDE identifies each calculated flight by joining the flight designator and an 8-digit number for the date flight (YYYYMMDD), such as for example, the flight from Madrid (ES) to Buenos Aires (AR) operated by Iberia Líneas Aéreas de España, S. A., or just Iberia (IB), that took place on Fri, Jun 10th, 2022, is internally coded in ACORDE as IB6845_20220610. Once the flight is correctly identified, ACORDE checks for its existence in several public databases and obtains the corresponding flight course track and all the publicly available data of the flight. Most online databases grant public access to the tracks for up to 90 days after the flight. However, commercial services provide private access for up to 3 years from the flight date[5]. Finally, all the gathered information is packed into a JSON file (`IB6845_20220610.json`) and stored in its own database for future reference.

Once the file containing the recorded track is obtained, the relevant information is obtained from a first analysis of the track, such as the arrival and departure airports and times, or the aircraft model. Then, the path is divided into three main stages: takeoff, cruise, and landing. Takeoff takes place between the time of the lift-off t_0 (provided) and up to the start of the cruise (not provided). The landing phase starts when the cruise ends (also not provided) and it is over at the moment of the touch down t_f (also provided). Then, the cruise phase is automatically determined by ACORDE by analyzing the recorded altitudes and their first time derivative. Immediately after the starting and ending times for the cruise are derived, the three stages of the flight are determined as well as the total duration of each one: Δt_t, Δt_c and Δt_l for the takeoff, cruise and landing respectively, and so, the duration of the flight $\Delta t = t_\mathrm{f} - t_0 = \Delta t_\mathrm{t} + \Delta t_\mathrm{c} + \Delta t_\mathrm{l}$. It is important to notice that aircraft operations at the origin and destination airports are not considered since these periods do not impact the total radiation exposure directly related to the flight.

The analysis of the track continues by defining N waypoints of the track, with N depending on the total duration of the flight, Δt. Each waypoint is defined by a four-dimensional vector $\vec{r_i} = (\phi_i, \lambda_i, h_i, t_i)$, where ϕ_i, λ_i, h_i and t_i are the geographic coordinates (latitude, longitude and altitude above sea level) and the UTC time of the i-esim waypoint. The first, $\vec{r_1}$, and last, $\vec{r_N}$, waypoints are defined at the middle point of the takeoff and landing stages, i.e., $t_1 = t_\mathrm{t} = t_0 + \Delta t_\mathrm{t}/2$ and $t_N = t_\mathrm{l} = t_\mathrm{f} - \Delta t_\mathrm{l}/2$ respectively. The second, $\vec{r_2}$, and the penultimate, $\vec{r_{N-1}}$ waypoints corresponds to the beginning and ending of the cruise stage of total duration given by $\Delta t_\mathrm{c} = t_{N-1} - t_2$. The cruise is then divided in segments of $\Delta t_i = t_{i+1} - t_i \simeq$

[5]See, for example, https://www.flightradar24.com.

600; 900 or 1800 seconds of duration for flight durations of up to 2 h (short flights), 4 h (intermediate flights) or > 4 h (long flights) respectively[6]. The exact duration of each step is then approximated by looking forward on having an integer total number of segments during the cruise. Each of these segments could be subdivided again if a change in the cruise altitude $\Delta h_i = h_{i+1} - h_i > 1,500\,\mathrm{ft}$ is observed during each particular step. Instead, if $\Delta h_i \leq 1,500\,\mathrm{ft}$, the altitude is fixed to the value where the flight stay more time during this segment. In case of doubt, it is always assumed $\Delta h_i = \max(h_{i+1}, h_i)$. Additionally, there are some moments where the actual time difference between two consecutive tracked points can be longer than the corresponding expected value for Δt_i, such as when the aircraft is flying above large unpopulated areas, or over the ocean and far from the continental shores or islands, or near to the poles. In those particular cases, the track is completed by assuming an orthodromic track[7] between the recorded extrema of these intervals, and then it is segmented using the same algorithm as for the recorded track. The altitude of the interpolated segments (it could be more than one) is fixed to the highest altitude between the two recorded values to always calculate the dose in the worst case scenario. The speed is calculated as the average speed for all the untracked distance along the orthodromic track (see Appendix A). Depending on the total duration of the flight Δt, the track could consist of up to $N \gtrsim 35$ waypoints for the longest cases using the default ACORDE configuration: 1 waypoint for each the takeoff and landing stages, plus $(t_\mathrm{c}/\Delta t_i) + 1$ for the cruise stage lasting t_c. As mentioned, Δt_i is slightly adjusted from the default configuration for having an integer number of segments. The dose is then calculated along the $(N - 3)$ segments between the waypoints at $\vec{r_i}$ and $\vec{r_{i+1}}$ with durations Δt_i for $i \epsilon [2, N - 1]$ (cruise) and for the takeoff and landing segments with durations $\Delta t_1 = t_1 - t_0$ and $\Delta t_{N-1} = t_{N-1} - t_\mathrm{f}$ respectively, and assuming the corresponding characteristics of these segments are those at $\vec{r_1}$ and $\vec{r_N}$. ACORDE also produces a `.DEG` file containing the same waypoints for the flight but in the format requested by the CARI7-A code, that will be used as the dose reference for each flight (see page 32 of [**?**]).

Once the waypoints have been obtained and the track has been seg-

[6]Of course, all these parameters can be easily changed in the ACORDE's configuration file.

[7]Also called the great-circle navigation track. See Appendix A for the detailed calculations performed.

mented, the local atmospheric profile corresponding to each waypoint $\vec{r_i}$ for that particular moment t_i is extracted from the Global Data Assimilation System (GDAS) database [36]. The Linsley's atmospheric model assumes the atmosphere is a mixture of N_2 (78.1%), O_2 (21.0%), and Ar (0.9%) and it is divided into 5 consecutive layers. In the lower four of them, the density varies exponentially with the altitude h, and so the mass overburden $X(h) = g\int_\infty^h \rho(z)\mathrm{d}z$, typically in units of $\mathrm{g\,cm^{-2}}$, is given by $X(h) = a_l + b_l \exp(-h/c_l)$ for $l = 1 \ldots 4$ [35]. For the fifth layer, typically for altitudes $h_5 \gtrsim 100\,\mathrm{km}$, it is assumed a linear variation with the altitude, $X(h) = a_5 - b_5 h/c_5$ that goes up to the altitude where $X(h) = 0$, typically reaching altitudes $h \gtrsim 110\,\mathrm{km}$ above sea level. The Linsley's coefficients at each waypoint $a_{l,i}$, $b_{l,i}$ and $c_{l,i}$, for $l = 1 \ldots 5$ are obtained by fitting the atmospheric density profile extracted from GDAS as explained in Grisales-Casadiegos et al. [4]. In this way, we assure to work with the most accurate atmospheric model possible within a 3-hour range containing t_i from the actual passage of the aircraft through $\vec{r_i}$. By the same way, we obtain the secular values of the Earth's magnetic field at $\vec{r_i}$ by using the current model of the International Geomagnetic Reference Field (IGRF) version 13 [**?**]. Local conditions and transient space weather phenomena that could affect the secular conditions of the geomagnetic field at $\vec{r_i}$ are also considered by accounting for the disturbances of the geomagnetic field and including the local geomagnetic rigidities and the effect of the Earth's magnetic umbra and penumbra using the method developed and described in Asorey et al. [1]. By following this method we are able to determine whether a simulated primary should or should not impinge in the atmosphere producing a shower, depending on its rigidity $R = Z\sqrt{E^2 - m^2}$, where Z, E, and m are the charge, total energy, and mass of the primary particle respectively. It is assumed in these calculations that the altitude and geomagnetic atmospheric conditions remain constant through the duration Δt_i of each segment.

Given the stochastic nature of the development of the EAS, which is also represented in the Montecarlo simulations performed to calculate the expected flux of secondary radiation along each segment, it is necessary to limit the effects of fluctuations that could affect or even dominate the radiation background composition estimation. So, the statistical significance of the calculation at each waypoint is increased by artificially enlarging the flight time for each step by the so called "coverage factor" κ of 9, 6, or 3 times for short, intermediate or long flights respectively, totaling a simulation time of 5400 s for each segment. Moreover, due to the Poissonian nature of the background calculations [?] the dose of each segment can be obtained simply by dividing each calculated dose by κ.

Once all this information is collected, all the corresponding files are packed and automatically transferred to one of the high performance computing (HPC) centres used for this calculation. The computations are performed inside Docker virtualised environments [?], the so-called Docker containers or simply containers, that are automatically instantiated and deployed within a physical cluster or a cloud-based virtualised cluster (vcluster), following the method developed by ?].

ACORDE computation relies on two different Docker images. The first one, called the ARTI Docker, is devoted to performing the calculations to obtain the expected flux of atmospheric radiation for each segment. Within this container, a pre-compiled instance of CORSIKA [?] v7.7402, compiled with QGSJET-II-04 [?] and GHEISHA [?] for the high and low energy interaction models respectively, and a specially modified version of the ARTI background simulation framework [?] are included. The third stage starts by deploying one container per track segment, that could sum up to $N-1$ simultaneous containers allocating the same number of nodes or v-nodes depending on the cluster capabilities. Within each docker, the expected flux of secondary background particles Ξ for each segment located at $\vec{r_i}$, namely Ξ_i, is calculated for a total integration time $\tau_i = \kappa \Delta t_i$ as explained in subsection 2.1. The main result of this third stage of the ACORDE workflow is to produce a single file, the so-called "*showers*" file (`.shw`), containing Ξ_i, i.e., all the secondary particles expected at $\vec{r_i}$, Ξ_i, per square meter during the time τ_i within the considered energy ranges used. Additional analyses are also performed producing, e.g., the lateral distribution functions of the secondary particles, i.e., the normalised particle number and the deposited energy E_d densities per type of secondary as a function of the distance to each shower axis, and the energy spectra of the secondaries per type of particle, as it will showed in section 3. Each step of the calculation is controlled by customised daemons included in the docker.

The fourth and last stage of ACORDE begins with the deployment of the DOSE docker, our second docker that it is devoted to dose calculations. As in the ARTI Docker, a special set of internal daemons controls the execution and reports the advance of the calculation through the different stages. Once the secondaries Ξ_i at $\vec{r_i}$ are obtained, these particles are propagated through a model of the aircraft vessel and a human phantom built in Geant4 [?]. It is also possible to simulate the integrated dose that should be expected by a

Gamma-Scout device [**?**] located in the cabin to perform comparisons with onboard measurements when corresponds. The aircraft fuselage is simply modeled as a cylinder of 5 meters long and the diameter of the plane in the passenger cabin, i.e., $d = 4.14\,\mathrm{m}$ for the case of the Airbus A320-200 [**?**], or 6.09ṁ for the case of the Airbus A350-900 [**?**]. As in the real airplane, the fuselage is modeled as a succession of three concentric and hollow cylinders of thickness $r_{e,j} - r_{i,j}$, where r_e and r_i corresponds to the external and inner radius of each hollow j-esim cylinder and the touching condition is obtained simply by doing $r_{i,j} = r_{e,(j-1)}$. Each layer ($j = 0, 1, 2$ for the external coverage, the thermal insulation layer, and the internal coating respectively) was modeled using the corresponding building materials. The cabin is then filled with dry air by considering a cabin altitude of $2,000\,\mathrm{m}$ a.s.l.($\sim 6,500\,\mathrm{ft}$), and standing in the cabin a simplified human phantom model based on the ICRP-110 Recommendations (**?**]) human phantoms for Geant4 applications by **?**] is placed.

It is important to remark at this point that the flux of cosmic rays is isotropic and homogeneous at the relevant energy scale for this calculation. So, even though all the secondary particles produced by the flux of cosmic rays in a given unit area at the top of the atmosphere will be distributed on a much larger surface at flight altitude, a sort of compensation process occurs. As detailed in [**?**], on average a secondary particle that misses the target area at ground by, say, 10 m to the East, will be compensated by a sib-similar secondary particle originated by a sib-similar primary impinging the upper atmosphere 10 m to the west. So, each secondary particle present in Ξ_i is then propagated from its initial velocity direction by the ACORDE Geant4 application through the aircraft and human phantom models, and all the relevant interactions, including mini showers that can be produced by the interaction of high energy secondaries with, e.g., the fuselage, are taken into account for the calculation of the absorbed dose. So, the deposited energy E_d during the i-esim segment of the track by each secondary particle j, identified in this case by the type of ionizing radiation[8] (R_j), is calculated for each one of the affected organs/tissues (T) of the phantom, and expressed as the absorbed dose ($D_{R_j,T,i}$) in units of gray (Gy, $\mathrm{J\,kg^{-1}}$). As the kind and energy of each particle are known, it is possible also to calculate from $D_{R_j,T,i}$ the equivalent ($H_{T,i}$) for the organ/tissue T, in units of sievert (Sv), by in-

[8]Currently, γ, $e^{\pm}$, $\mu^{\pm}$, n, p, α, other nuclei and other hadrons.

cluding the radiation weighting factors (w_R) that take account of the relative biological effectiveness (RBE) of the different types of ionising radiations, i.e., $H_{T,i} = \kappa^{-1} \sum_j \sum_{R_j} w_{R_j} D_{R_j,T,i}$, where the summation in j runs over all the secondary particles of the i-esim segment of duration $\Delta t_i = \tau_i/\kappa$. In this sense, $H_{T,i}$ represents the equivalent dose deposited at each organ/tissue by the total flux of secondary particles during the segment i-esim of the track impinging that organ/tissue. As the effective dose E is the main ICRP quantity in terms of radiological protection [**?**], E_i is determined from $H_{T,i}$ following the ICRP 103 recommendations [**? ?**], i.e., $E_i = \sum_T w_T \sum_T H_{T,i}$, where w_T is the tissue weighting factor, "that approximates its relative contribution to the overall detriment from uniform whole-body irradiation by sparsely ionising radiation" [**?**]. So, E_i is the effective dose, also in units of sieverts, integrated for the segment i-esim of the flight track. This process is repeated for each segment of the track, and the total effective dose is then calculated by summation, $E = \sum_i^{N-1} E_i$, and the same for D, H and B_R, where B_R is just the integrated number of secondary particles per radiation type.

3. Results

To test the effectiveness of ACORDE, the total effective dose received in more than 300 flights was calculated by using the above described methodology. As mentioned, the dose for the same flights was also calculated using CARI7-A with the standard configuration and using the same path that was used to perform ACORDE calculations to reduce the source of possible differences. Most of the studied flights in this work are from Iberia, IATA call sign IB, as it operates mainly within Spain and several international destinations in Europe and America, with some particular flights operated by Iberia under the call sign of Finnair (AY). For the dates included in this study, Iberia flights to and from Asia were suspended due to the COVID-19 pandemic. Thus, additional flights operated by Japan Airlines, IATA call sign JL, and Cathay Pacific, IATA call sign CX, were also included for studies on tracks related to geomagnetic disturbances due to Solar Activity that could affect the dose during a near-pole flight. It is obvious to mention that this methodology can be extended to any airline, route, and date.

3.1. A complete example on how ACORDE performs

To better illustrate the way in which the results have been obtained with a specific example, let us consider the flight IB3270_20211116 operated by Iberia and flying from the Madrid Barajas Airport (MAD) to the Hamburg Airport (HAM) in an Airbus A320 (A320-216 EC-LXQ). The flight reported departure and arrival times at 11:43:50 CET and 14:20:46 CET respectively, with a total duration of 2h36m56s ($9,416\,\mathrm{s}$). However, according to the flight track, the actual takeoff and landing occurred at $t_0 = 11/16/2021\ 10:44:40\,\mathrm{CET}$ and $t_\mathrm{f} = 11/16/2021\ 14:19:31\,\mathrm{CET}$ respectively, for a total duration of $\Delta t = 9,291\,\mathrm{s}$. ACORDE determined that the cruise altitude ($h_2 = 36,000\,\mathrm{ft}$ for the first segment) was reached at $\Delta t_\mathrm{t} = 1,375\,\mathrm{s}$ after the takeoff, and the cruise duration was of $t_\mathrm{c} = 6,370\,\mathrm{s}$. As this is an intermediate flight, the duration of each segment was adjusted to $\Delta t_i = 910\,\mathrm{s}$ (15m10s), resulting in $N = 10$ waypoints (eight for the cruise, including the corresponding starting and ending cruise waypoints, and 2 at the intermediate points of the takeoff and landing stages) and 9 segments where the dose was calculated. For this flight, the coverage factor was set to $\kappa = 6$, so the total flux integration time for each segment was $\tau_i = 5,460\,\mathrm{s}$. The flight track and the determined waypoints of the flight are shown in figure 1.

Once the waypoints were identified, the atmospheric profiles at $\vec{r_i}$ are extracted from the GDAS database, and the Linsley's model is used to obtain the coefficients a_l, b_l and c_l, and the transition altitude h_l of each of the five atmospheric layers. With them, the atmospheric profiles are characterised and the density $\rho(h)$ and the mass overburden $X(h)$ as a function of the altitude are obtained. In figure 2, the reconstructed $X(h)$ for the seven segments of the cruise stage of the flight IB3270_20211116 are shown as well as the US standard model typically used as the reference for this kind of calculations. Slightly but important differences can be observed between the different local profiles bearing in mind the effect on the development of the atmospheric radiation Ξ_i is not only local, but mainly depends on the integral from the top of the atmosphere to the altitude of the segment. Moreover, the differences are largely increased when each of these profiles are compared with the standard atmospheric profile: at $h = 37,000$ the difference between X_2 and X_Std is of $12.5\,\mathrm{g\,cm^{-2}} \simeq 1.3\,\mathrm{kPa}$ ($\sim 5\%$), and this kind of differences can be of more than 10% for near-polar flights [**?**]. No significant geomagnetic disturbances were observed during the flight, so the secular values of the geomagnetic field as well as the local rigidity cutoff tensor were calculated

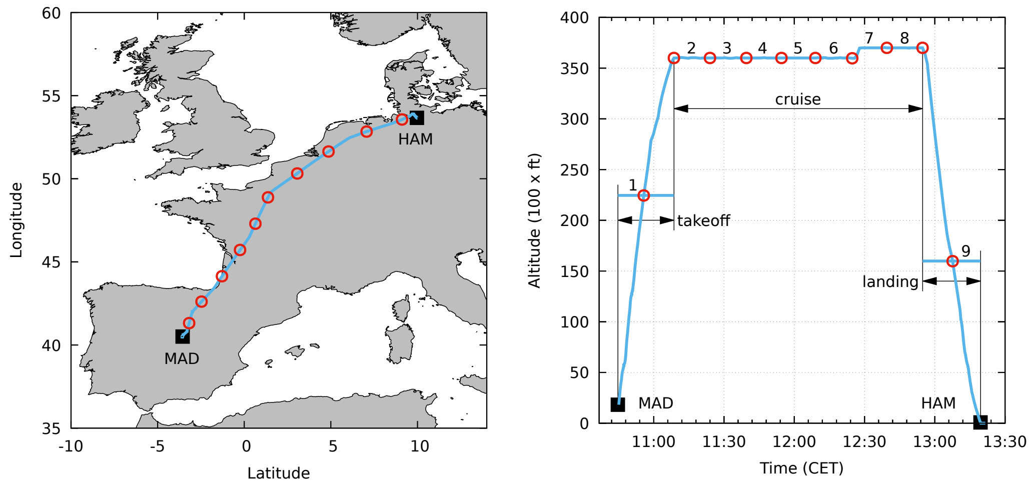

Figure 1: Left: Real track (light blue line) of the flight IB3270 that flew from MAD to HAM (black squares) on November 16$^{\text{th}}$, 2021. ACORDE determined the start and the end of the cruise stage and calculated the waypoints were the dose had to be calculated (red circles). See the text for the details. Right: Airplane altitude as a function of time (light blue line) and the waypoints (red circles) automatically identified by ACORDE as well as the three stages of the track: takeoff, cruise, and landing. As explained in the text, for this calculation it is assumed that the altitude for the takeoff and the landing are the ones at the half time of the corresponding stage. The segments where the onboard dose was calculated are identified by their corresponding number. See the text for further details.

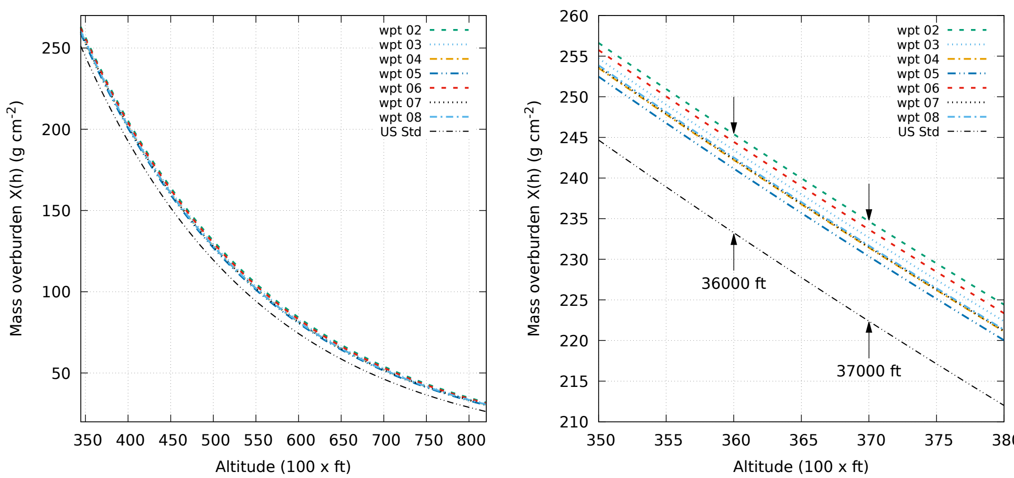

Figure 2: The atmospheric mass overburden $X(h)$ as a function of the altitude h for the seven cruise segments of the flight IB3270 of November 16$^{\text{th}}$, 2022, between levels 350 and 800 (left) and at flight altitude (right). It was obtained from the atmospheric profiles extracted from the GDAS database as explained in the text. For comparative reasons, the mass overburden of the US Standard atmosphere is also shown. The observed difference between the locals and the US standard atmospheric profiles at the flight altitudes is of $\sim 1.3\,\text{kPa}$ ($\sim 5\%$).

using only the IGRF-13 as explained in Asorey et al. [1].

ACORDE collected and prepared all this information, and it was used within the ARTI docker to calculate the flux of expected secondary particles along each flight segment Ξ_i within the current energy ranges. While the flux is dominated by electromagnetic particles, when considering the dose this may not be the case taking into account the RBE for each type of particle. In the right panel of figure 3 the evolution of $\Xi_{i,j}$ along the flight track is shown for the different types of particles j: photons and electrons, muons, neutrons and nuclei and other hadrons, and also the secondary momentum distribution of Ξ_1 (takeoff) and Ξ_2 (cruise first segment) are shown as well as the integrated value of $\Xi_{i,j}$ for each flight segment and type of particle. It is clearly visible the altitude effect on Ξ_i, both in terms of atmospheric absorption and in the development of the EAS, with up to more than two orders of magnitude in the neutron flux when compared with similar spectra at ground level. As an example, the flux of particles at ground level typically ranges between 700 and $2,000\,\text{m}^{-2}\,\text{s}^{-1}$ within this energy range [?], while the average flux of particles impinging this particular flight was of $6.5 \times 10^4\,\mathrm{m^{-2}\,s^{-1}}$ and reached the maximum value of $9.3 \times 10^4\,\mathrm{m^{-2}\,s^{-1}}$ for the segment $i = 8$. The total figures are also impressive: during the flight, among others, about 3.7×10^3 neutrons, 1.2×10^3 protons and 4.2 nuclei with kinetic energies $E > 50\,\mathrm{MeV}$, and 5×10^4 photons and 5.4×10^3 electrons and positrons with $E > 50\,\mathrm{keV}$ impinge each cm^2 of the aircraft and interacted with the fuselage, the avionics, and the people inside the plane.

Once the secondaries for each segment were obtained, the DOSE docker is deployed and the file containing Ξ was injected to calculate and integrate the effective dose for each segment, following the procedure described in section 2.2 according the ICRP 103 recommendations [**?**]. Hence, the total effective dose for this flight obtained with the ACORDE framework was of $E_\mathrm{A} = 11.6\,\mu\mathrm{Sv}$. As mentioned, ACORDE also produces a waypoint file compatible with CARI7-A, so the latter was used to also obtain a reference dose for each flight. In this case, the dose calculated by CARI7-A in the standard configuration was $E_\mathrm{C} = 9.2\,\mu\mathrm{Sv}$. So, the observed differences in the calculated dose between ACORDE and CARI7-A are $\Delta E = E_\mathrm{A} - E_\mathrm{C} = 2.4\,\mu\mathrm{Sv}$ and $\Delta E_{\%} = 2\,(E_\mathrm{A} - E_\mathrm{C})\,/\,(E_\mathrm{A} + E_\mathrm{C}) = +23\%$ for this particular flight.

3.2. Extended analysis

All the described calculations were performed for 287 randomly selected flights operated by Iberia, plus 37 particular flights operated by Finnair, Japan Airlines, and Cathay Pacific that were selected to evaluate the ACORDE performance during a solar activity period, as described in subsection 3.3. The obtained results are provided as a set of "tab separated values files" (`.tsv`) as supplementary material for this article **[NEED REF]**. In these files, the resulting effective doses E_C and E_A calculated by using CARI7-A in the standard configuration and ACORDE respectively are stored for the complete dataset, and for both the separated subsets described above. In this section we provide a comparative analysis of the whole dataset. However, it is important to recall that each flight should be considered essentially unique, as even for the same route, the real track could be modified by meteorological reasons, crowded routes or operative reasons, and these alterations could have a significant impact on the total dose, especially for changes related to the flight altitude as it will be described in subsection 3.5. Even more, local changes in the atmospheric and geomagnetic conditions, or the usage of a

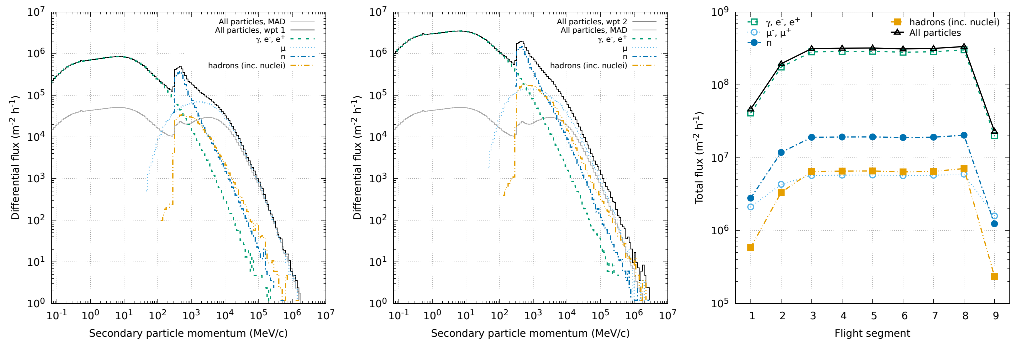

Figure 3: The momentum p_s spectrum of the secondary particles that are expected for the flight IB3270_20211116 during the takeoff segment at an altitude of 22,450 ft (left), and during the first cruise segment $\vec{r_2} \rightarrow \vec{r_3}$ at an altitude of 36,000 ft (center). The main components of the background radiation, i.e., the electromagnetic component (dashed green line), the muons $\mu^{\pm}$ (dotted light blue line), neutrons (dashed dot blue line), and other hadrons including nuclei (double-dot dashed yellow line) are identifiable by their own characteristics as described in section 2. The altitude effect on the flux of the different types of particles is clearly visible by comparing these two figures and when comparing with the corresponding distribution for the total differential flux at MAD (gray solid line). The evolution of the integrated flux along the flight is shown on the right-hand side for the different components as well as for the total flux.

different aircraft vessel, could have a significant impact on the internal secondary particles distribution and the corresponding effective onboard dose. While all these factors are considered in most of the dose calculation codes including ACORDE, they can be assessed in different ways and could then produce different final results.

As explained in the section 2.2, all the analysed flights were separated into three categories depending on the flight duration, and labeled as 1, 2 and 3 for short, intermediate, and long flights respectively. As it is shown in table 1, when comparing the obtained values for E_{A} and E_{C} within each category some systematic differences raised. While it is important to remark that this comparative averaged analyses is limited for the above described reasons, for the three categories the differences between the doses calculated by ACORDE are, in average, larger than the ones calculated with CARI7-A, in particular for long flights. For short and intermediate flights, the averaged absolute differences are compatible with zero within 1-sigma confidence interval. However, while the absolute differences are in the range $[1.9, -1.3]\,\mu$Sv and $[8.6, -4]\,\mu$Sv for short and intermediate flights,

Table 1: Average differences between the total effective doses calculated with ACORDE, $E_{\rm A}$, and CARI7-A, $E_{\rm C}$, for the three flight categories described in the text: short (1), intermediate (2), and long (3) flights. The average absolute differences, $\langle \Delta E \rangle = \langle E_{\rm A} - E_{\rm C} \rangle$, and the corresponding relative differences, $\langle \Delta E_{\%} \rangle = \langle 2\,(E_{\rm A} - E_{\rm C})\,/\,(E_{\rm A} + E_{\rm C}) \rangle\,\%$, are expressed in units of μSv and percents respectively, as well as the maximum and minimum values of both magnitudes. For producing the last two rows ($3^{\dagger}$ and $3^{\ddagger}$), the 37 long (type 3) routes described in subsection 3.3 were calculated apart to evidence the impact of these particular flights. Q stands for the number of flights calculated.

Type	Q	$\langle \Delta E \rangle$	$\max(\Delta E)$	$\min(\Delta E)$	$\langle \Delta E_{\%} \rangle$	$\max(\Delta E_{\%})$	$\min(\Delta E_{\%})$
1	153	(0.3 ± 0.6)	1.9	-1.3	(11.4 ± 21.4)%	49.4%	-54.1%
2	58	(1.2 ± 2.4)	8.6	-4.0	(12.5 ± 23.7)%	70.1%	-40.0%
3	113	(30.1 ± 22.1)	64.5	-19.0	(43.5 ± 36.5)%	101.8%	-50.7%
$3^{\dagger}$	76	(21.7 ± 21.2)	50.1	-19.0	(41.2 ± 44.3)%	101.8%	-50.7%
$3^{\ddagger}$	37	(47.5 ± 10.9)	64.5	25.8	(48.2 ± 5.1)%	57.7%	36.6%

the observed relative differences could reach up to $+50\%$ and $+70\%$ in these categories when comparing the dose obtained by ACORDE with the one obtained using the same waypoints in the standard configuration of CARI7-A. The systematic differences are enlarged for the long range flights, where we observed a significant absolute excess of $\langle \Delta E \rangle = (+30.1 \pm 22.1)\,\mu$Sv and relative $\langle \Delta E_{\%} \rangle = (+43.5 \pm 36.5)\%$, with the doses observed ranges between $-19\,\mu$Sv and $+64.5\,\mu$Sv for the same absolute differences, and relative differences between -50.7% and 101.8%. However, when the 37 special flights are separated from the rest of the 287 flights, the observed average absolute difference in these long flights is reduced, as it can be seen in the last rows of table 1 (types 3, $3^{\ddagger}$ and $3^{\dagger}$ respectively) and is explained in the next subsection.

3.3. Analysis of some long West-East-West flights

Between the end of October and the beginning of November 2021, a period of high solar activity was reported after the solar active region identified as NOAA 2887 produced some M-class flares and an X1 flare on Oct $28^{\rm th}$, hence generating the ground level enhancement GLE73 with some geomagnetic storms recorded on $\rm Oct^{st}$, and releasing a slow interplanetary coronal mass ejection (iCME) pointing to Earth on Nov 1st. A few hours later, the NOA 2891 active region produced a fast iCME that also pointed to Earth and interacted in the interplanetary space with the slower NOAA 2887 iCME resulting into a complex structure that arrived to Earth on November 3rd at 19:24 UTC, producing geomagnetic disturbances with observed DST (disturbance storm index) [?] of $-5\,$nT. The reader is referred to the work by ?] about the complex interactions observed. To evaluate the ACORDE performance during these particular events, 37 particular flights that flew between October 22nd, 2021 and November 21st, 2021 have been studied. Thus, these particular routes were affected by the aforementioned high solar activity: CX843 (JFK-HKG), CX829 (YYZ-HKG), JL42 (LHR-HND) in the Europe to Asia direction, and CX844 (HKG-JFK), CX826 (HKG-YYZ) and JL41(HND-LHR) in the reverse one. In the type $3^{\ddagger}$ row of the table 1, the comparative analysis between the doses calculated with ACORDE and CARI7-A are shown. Large absolute and relative average differences, $\langle \Delta E \rangle = (47.5 \pm 10.9)\,\mu$Sv in the range $[+25.8, +64.5]\,\mu$Sv, and $\max(\Delta E_{\%}) = (48.2 \pm 5.1)\%$ in the range $[36.6, 57.7]\%$ between both methods for these 37 flights can be observed. In figure 4, the time evolution of both the calculated doses with ACORDE and CARI7-A are shown for the studied routes. As mentioned in the previous section, the geomagnetic disturbances, tracks, cruise altitude, and atmospheric conditions change from flight to flight even for the same routes. However, while important positive differences are observed between ACORDE and CARI7-A, which are even larger when this solar activity reaches the Earth, the global evolution within each route is approximately preserved. The table containing all the information of these flights is included in the supplementary material of this work **[NEED REF]**.

3.4. Paving the way for a future experimental verification of ACORDE

As mentioned in section 2, ACORDE includes a module for the simulation of the expected doses that can be registered by a Gamma-Scout [?] installed onboard the aircraft and placed in close contact with the internal surface of the cabin. The Gamma-Scout is a dosimeter that is actively used in several industries to determine environmental radioactive doses. It allows the measurement of $\alpha-$, $\beta-$ and $\gamma-$radiation thanks to an LND end-window[9] cylindrical counting Geiger-Müller (GM) tube of 9.1 mm in diameter and 38.1 mm in length. Without shielding, it is able to measure αs with $E_{\alpha} > 4\,$MeV, electrons with $E_e > 200\,$keV, and photons with $E_{\gamma} > 30\,$keV. A special mechanical selector can be used to place an aluminium sheet of 3 mm thick to

[9] Typically made of muscovite (mica), with $X \simeq 1.5 - 2 \times 10^{-3}\,\mathrm{g\,cm^{-2}}$ and simulated as a mixtures of 50% of SiO_2, 35% of Al_2O_3, 10% of K_2O, 4% of Fe_2O_3 and 1% of Na_2O.

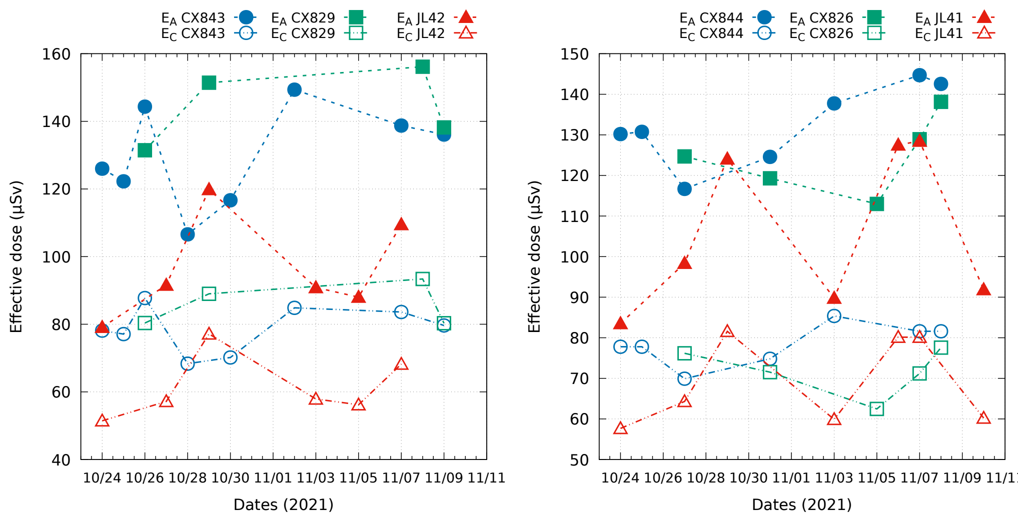

Figure 4: Temporal evolution of the doses calculated by using ACORDE (filled symbols, dashed lines) and CARI7-A (empty symbols, dotted-dashed lines) for 37 flights covering routes between Europe to Asia (left) and Asia to Europe (right) during a high solar activity period by the end of October and the beginning of November 2021. It is important to notice that tracks, cruise altitudes, and the atmospheres varies from flight to flight, even for those serving the same route.

block all the α particles and electrons with $E_e < 2\,\text{MeV}$, an aluminium foil of 0.1 mm thick shielding only the $\alpha-$radiation, or leave the window open for simultaneously measuring the three types of radiation. For defining the calibration constants of the simulated device only the tube was simulated and it is assumed the detector is operated with the measurement windows totally open. As for the calibration of the physical device, we simulate three different sources of ^{137}Cs, ^{60}Co, $^{99\text{m}}$Tc, and ^{18}F sources with an spherical emission placed at 1 m in air of the simulated device in the open window configuration and adjusted the corresponding calibration constants of the Metropolis Monte Carlo algorithm up to obtaining the figures reported in pages 68–69 of [**?**]. For example, an effective dose rate of $86\,\mu\text{Sv}\,h^{-1}$ for the 1 GBq ^{137}Cs source was obtained. Once the calibration parameters were obtained, we irradiated the simulated dosimeter in the open configuration with photons of $E_\gamma = 662\,\text{keV}$ (^{137}Cs) and observed that a rate of 150 CPM (counts per minute) corresponded to an effective dose rate of $1\,\mu\text{Sv}\,\text{h}^{-1}$ (please see page 43 of [**?**]). Thus, once the simulated detector is properly calibrated, we are able to estimate the expected dose rate for each segment of the flight and the total integrated dose. So from the flux of atmospheric radiation at each segment, we select only γ, $e^{\pm}$ and α within the corresponding energy range[10] and the detector calibration take place by using the same DOSE docker as for the effective dose in humans. In the table 2 the obtained doses are shown for some selected flights. It is important to notice that both ACORDE and CARI7-A estimate the effective doses by using the response to all the radiation present in the atmospheric radiation. However, as any other GM tube (where the measurement of the energetic particles detection is strongly suppressed) neutrons are not detected since these particles does not ionise the gas. For these reasons, the total dose measured by a Gamma-Scout or any similar device will be lower than the dose calculated by considering all the atmospheric radiation effects including muons, energetic particles and specially neutrons. By design, ACORDE is able to predict the expected dose that a commercial GM based dosimeter could measure onboard the aircraft in exactly the same circumstances as the total effective dose is determined, opening an easy way to test ACORDE predictions by following an standard procedure in the aviation industry and avoiding the necessity of installing

[10]In this version of ACORDE, the lower energy limit for the simulated photons is 50 keV instead of 30 keV.

other types of detectors that could affect the normal operation of the flight (despite they are a much more precise way that determine the total effective dose than a simple commercial GM-based dosimeter).

Table 2: Expected effective doses calculated by using ACORDE and CARI7-A for some selected flights, including the expected dose as it should be measured by a Gamma-Scout (GS) device onboard the aircraft close to the internal surface of the cabin. Total effective doses are expressed in units of μSv.

T	Flight	Date	E_{A}	E_{C}	GS	T	Flight	Date	E_{A}	E_{C}	GS
2	IB3058	20210903	12.5	11.5	5.2	3	IB6177	20211211	100.1	68.0	49.1
2	IB3059	20210903	11.5	10.8	4.2	3	IB6178	20211212	93.9	63.6	49.8
3	CX0843	20211024	126.0	78.1	43.7	3	IB6250	20210904	42.5	30.4	17.9
3	CX0844	20211024	130.2	77.8	48.0	3	IB6251	20210901	45.0	33.4	19.0
3	IB6011	20211128	45.4	33.1	26.2	3	IB6453	20210707	33.0	41.0	19.8
3	IB6012	20211130	47.9	32.5	28.0	3	IB6454	20210709	32.0	40.0	18.0

Summarizing, it will be easy to experimentally estimate if ACORDE provides accurate results by comparing the values simulated with this code running under the Gamma-Scount module (labeled as GS in table 2) and a real measurement with any present-day Gamma-Scout detector installed in an airplane. Might this hypothesis be confirmed, it could be derived that the ACORDE estimation of the dose absorbed taking into account only the $\alpha-$, $\beta-$ and $\gamma-$radiation (GS again) is correct and, consequently, the estimation of ACORDE under the module which takes into account the whole spectrum of radiation (E_{A}) will be potentially valid as well.

3.5. Impact of the cruise altitude in the total dose

While the atmospheric and geomagnetic conditions could produce measurable changes in the calculated values of the doses in the aircraft, the most important effect is related to changes in the cruise altitude during the flight. As an example of the ACORDE capabilities for calculating the dose in different conditions, we evaluate the evolution of the dose as a function of the altitude both in ACORDE and in CARI7-A by changing the cruise altitude between $30,000\,\text{ft}$ and $44,000\,\text{ft}$ in steps of $2000\,\text{ft}$ for the flights IB6177_20211211 (MAD-LAX) and IB6178_20211212 (LAX-MAD). The rest of the conditions of both flights and the selected waypoints were preserved to avoid other possible sources of variations, such as those introduced by different atmospheric or geomagnetic conditions. In figure 5 the recorded track and the waypoints used for the track completion are shown for the original

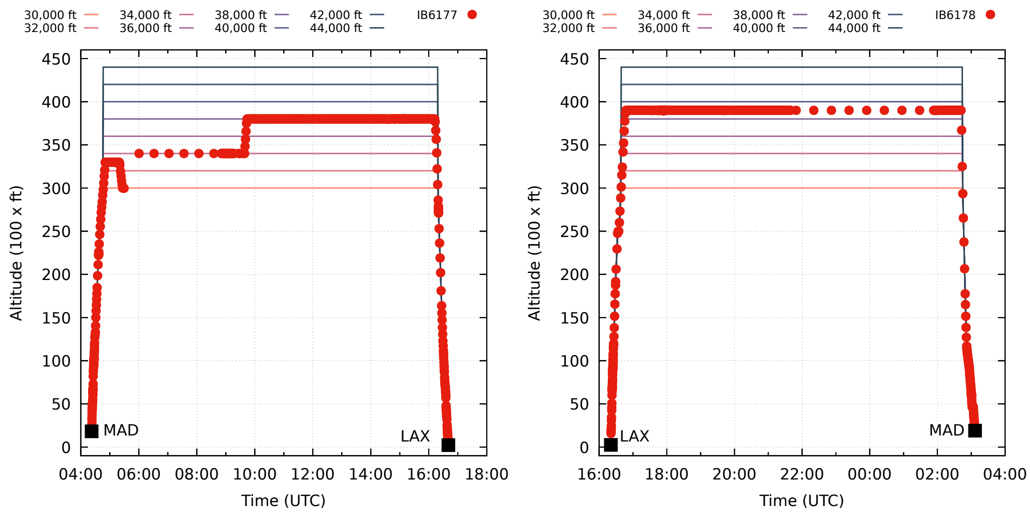

Figure 5: Recorded and modified tracks for the flights IB6177 (MAD-LAX) and IB6178 (LAX-MAD) of December, 11$^{\mathrm{th}}$ and 12$^{\mathrm{th}}$ 2021. The original track (red circles) has been artificially modified to evaluate the effect of the altitude on the effective dose when all the other conditions remain unaltered, resulting in the tracks with cruise altitude from $30,000\,\mathrm{ft}$ to $44,000\,\mathrm{ft}$ every $2,000\,\mathrm{ft}$ (coloured solid lines). The unrecorded segments of the cruise above the Atlantic ocean and the reconstructed path are noticeable at the beginning (IB6177) and ending (IB6178) of the tracks, as the waypoints are separated by $\Delta t_i = 1857\,\mathrm{s}$ and $\Delta t_i = 1877\,\mathrm{s}$ respectively. See section 2.2 for further information about the completion procedure.

recorded and the modified tracks. It is clearly visible the different evolution of both flights: while the IB6178 remained at a constant altitude of $39,000\,\mathrm{ft}$ for almost all the cruise stages, the IB6177 altitude had some changes along its track.

Figure 6 and table 3 summarise the results of this altitude variation study. It is clearly noticeable the altitude effect on the total effective dose calculated both in ACORDE and in CARI7-A. Important differences, of up to a factor of more than 3, can be observed for both flights in the reconstructed doses when comparing their value as the altitude changes between $30,000\,\mathrm{ft}$ and $44,000\,\mathrm{ft}$, the current maximum altitude that the new generation of airplanes can reach.

3.6. ACORDE computing performance

As mentioned in section 2.2, ACORDE relies on a large amount of computing power to perform the described Monte Carlo simulations on a flight-

Table 3: Cruise altitude effect over the total effective dose for both the studied flights IB6177 and IB6178. Important differences up to a factor of $\gtrsim 3$ in the dose can be observed between cruise altitude of 30,000 ft and 44,000 ft. The doses of the original flights are also included.

Flight	Date	Alt	E_A	E_C	Flight	Date	Alt	E_A	E_C
IB6177	20211211	orig	100.0	68.0	IB6178	20211212	orig	93.9	63.6
IB6177	20211211	30000	57.6	42.0	IB6178	20211212	30000	43.5	33.1
IB6177	20211211	32000	71.4	50.5	IB6178	20211212	32000	53.0	39.5
IB6177	20211211	34000	86.1	59.6	IB6178	20211212	34000	64.2	46.4
IB6177	20211211	36000	102.4	69.2	IB6178	20211212	36000	77.6	53.6
IB6177	20211211	38000	117.8	79.3	IB6178	20211212	38000	91.3	61.1
IB6177	20211211	40000	137.3	89.8	IB6178	20211212	40000	105.2	68.7
IB6177	20211211	42000	154.9	100.4	IB6178	20211212	42000	122.7	76.2
IB6177	20211211	44000	172.6	110.9	IB6178	20211212	44000	136.3	83.7

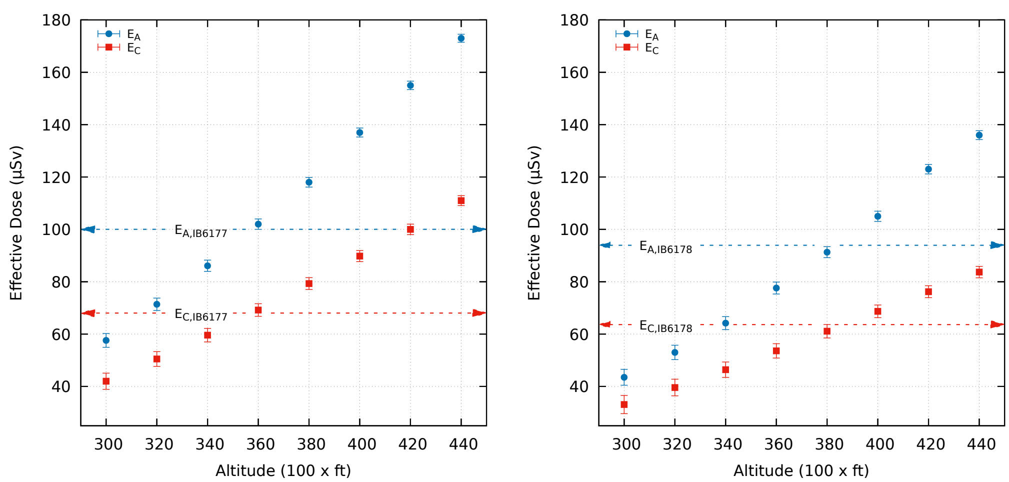

Figure 6: Effective dose as a function of the cruise altitude of the modified flights IB6177 (MAD-LAX) and IB6178 (LAX-MAD) of December, 11$^{\text{th}}$ and 12$^{\text{th}}$ 2021, as it was determined by ACORDE (blue circles) and with the standard configuration of CARI7-A (red squares). As a reference, the doses calculated for the original flights are indicated by the respective arrows.

by-flight basis. For this reason, the codes are prepared to run within docker containers that can be deployed in high-performance computing facilities, small clusters running at Universities, and distributed environments running on public clouds, such as AWS or Google Cloud, and federated ones, such as the European Open Science Cloud [?]. However, the code that controls the global execution of the calculations can run on a standard personal computer.

The calculation starts from a file containing the list of all the ACORDE codes of the flights that need to be calculated. ACORDE reads the file, identifies the corresponding flights, checks for their existence and the existence of the information in flight databases, and gathers all the information related to the flight, including the track. All the information is combined to obtain the waypoints for the segmented track (both in ACORDE and CARI7-A format), and the instantaneous atmospheric profiles and geomagnetic conditions for each waypoint. The data is then packed and, by using the corresponding keys or access tokens, it is transferred to either HPC or cloud-based facilities facilities, where the dockers are deployed as described before, the Monte Carlo simulations start, and are further controlled by local daemons within the docker containers. The final result consists of a collection of different files containing all the required information, essentially, a JSON file containing lists with the values for the local E_i, H_i, D_i and $B_{R,i}$, the total values of all the doses E, H, D, B_R, and the dose calculated by CARI7-A using the standard configuration. All these files and the `.DEG` file, are then transferred back to the ACORDE main code for the final integration and preservation of the results. All the information needed to completely reproduce the calculation is securely stored for reproducibility matters. The larger files, such as those containing the secondaries reaching each waypoint, are also stored in a cloud storage for further analysis. While the overall file sizes will depend on the track conditions and the altitude changes during the flight, as a rule of thumb and on average, the simulation requires a total storage of about $\approx 6\,\mathrm{GB}$ per hour of flight of heavily compressed binary files. However, given that the showers files can be exactly recovered by re-running again the simulation using the same inputs as for the original calculation, the storage needs are largely reduced down to $\lessapprox 1\,\mathrm{MB}$ per hour of flight of uncompressed files and $\approx 100\,\mathrm{kB}$ per hour when compressed. Regarding the computing power required, again it will also depend on the exact track (specially the altitude), and of course on the computing system used. In common HPC clusters running processors based on the Intel 6240 at 2.6GHz and 100 Gb/s connection network, the total computation time, including the preliminaries, the EAS developments, and the dose calculations can be estimated as $\sim 7-9$ CPU·hours per hour of flight.

4. Conclusions and future perspectives

In this work, the methodology and capabilities of the *Application COde for the Radiation Dose Estimation* (ACORDE) are presented. ACORDE is a new code that integrates the current state-of-the-art Monte Carlo simulation codes for the interaction of cosmic rays with the atmosphere, in general for the interaction of radiation with matter, and for estimating the effective dose that the crew and passengers could receive being onboard of a commercial flight. By gathering the available information of the flight, including the real track of the plane, ACORDE identifies the main characteristics of the route and divides the track in segments of predefined duration. For each segment, the local atmospheric and geomagnetic conditions are determined and these data are then used to determine the flux of atmospheric radiation expected at each segment. Then, this flux is propagated in Geant4 models of the plane and a human phantom to calculate the effective dose following the last ICRP recommendations [**?**]. With ACORDE it is also possible to intentionally vary the track and altitude for comparative reasons, and to calculate the expected radiation that commercial dosimeters installed onboard the cabin would measure in exactly the same conditions as the total effective dose for the flight was calculated. As a reference, in this work the total dose for each analysed flight is also calculated with CARI7-A in the standard configuration and by using the same waypoints that were used to define the ACORDE segmentation.

To assay ACORDE capabilities, a total of 324 flights covering very different routes mainly starting from Spain were analyzed. Accordingly, the flight duration is identified as a short (< 2 h), an intermediate (< 4 h) or a long (> 4 h) flight. In some flights very significant differences were observed between the doses calculated with ACORDE and CARI7-A, in particular for the case of long west-east-west routes. Moreover, ACORDE dose estimation is, on average, systematically larger than the corresponding CARI7-A effective dose, specially when constrained to the long flights category. While each flight should be considered essentially unique, the observed absolute and average differences between the effective dose calculated with ACORDE and CARI7-A remain and are compatible with zero within the systematic error bars in the three studied group. This is not the case when the 37 long west-east-west analyzed routes that flew during a period of high solar activity are included.

By using ACORDE commercial dosimeters simulations capabilities, these discrepancies could be resolved by a measurement campaign based on compact non-gaseous neutron detectors and commercial GM dosimeters as those regularly used in the industry.

Starting only from the list of flights to be analysed, the current version of ACORDE (1.0.0) is able to run on a single desktop computer and to command and control all the required simulations that could be performed on small local clusters or large HPC and cloud-based public and federated infrastructures in an autonomous and unsupervised way. Future versions of ACORDE will include several capability improvements, such as: the enhancement of the fuselage model including inner structural and internal elements that could slightly affect the total shielding (such as stringers or the hand luggage in the cabin); both the complete human male and female ICRP-110 phantoms; an extension based on CORSIKA and FLUKA of the atmospheric neutrons energy range down to the epi- and thermal energy ranges; and, the integration of the blockchain technology for reproducibility and traceability of all the information collected and produced in all the calculation stages of ACORDE.

Acknowledgments

This work was partially funded by the 'European Open Science Cloud-Expanding Capacities by building Capabilities' (EOSC-SYNERGY) project, funded by the European Commission' Horizon 2020 RI Programme under Grant Agreement nº 857647. and by the Comunidad de Madrid CABAHLA-CM project (S2018/TCS-4423).

Appendix A. Orthodromic tracks

Orthodromic tracks, also called great-circle tracks, allow the calculation of the track that minimizes the distance to travel between two points on a spherical surface. In this work, we assumed an orthodromic track to connect those points when the temporal distance is bigger than the required temporal coverage for each type of flight. That could be the case when the plane flies over large unpopulated areas, close to the Artic, or over the oceans. In these cases, given the last and first consecutive registered points of the track, identified by their geographical and time coordinates $(\phi_1, \lambda_1, h_1, t_1)$ and $(\phi_2, \lambda_2, h_2, t_2)$ for the latitude, longitude, altitude and time respectively, the total distance travelled is given by

$$d_{1,2} = R_\oplus \Delta\sigma = R_\oplus \arctan \frac{\sqrt{(\cos\phi_2 \sin(\delta\lambda))^2 + (\cos\phi_1 \sin\phi_2 - \sin\phi_1 \cos\phi_2 \cos(\Delta\lambda))^2}}{\sin\phi_1 \sin\phi_2 + \cos\phi_1 \cos\phi_2 \cos(\Delta\lambda)}, \tag{A.1}$$

where $\Delta\lambda = |\lambda_1 - \lambda_2|$ and to minimize the errors due to the non-spherical shape of the Earth, it is considered a sphere of radius $R_\oplus = \frac{1}{3}(2R_{\text{eq}} + R_{\text{pol}}) \simeq 6,371\,\text{km}$, where R_{eq} and R_{pol} are the equatorial and polar Earth's radius for the WGS84 geoid. This approach could introduce an error in the total length of the track no greater than 0.5%. When h_1 and h_2 are different, it is considered that all the unregistered path was travelled at $\max(h_1, h_2)$ to consider the worst case scenario. Alternatively, an interpolated altitude track can be also considered. Thus, the average linear and angular velocities are simply given by $v_{\text{avg}} = d_{1,2}/(t_2 - t_1)$ and $\omega_{\text{avg}} = \Delta\sigma/(t_2 - t_1)$. Once the untracked track is defined, the waypoints over the track are obtained following the same algorithm as for the known track, using the averaged speed and altitude defined by this assumption.

References

[1] H. Asorey, L. A. Núñez, M. Suárez-Durán, Preliminary results from the latin american giant observatory space weather simulation chain, Space Weather 16 (2018) 461–475.

[2] T. Böhlen, F. Cerutti, M. Chin, A. Fassò, A. Ferrari, P. G. Ortega, A. Mairani, P. R. Sala, G. Smirnov, V. Vlachoudis, The fluka code: developments and challenges for high energy and medical applications, Nuclear data sheets 120 (2014) 211–214.

[3] P. K. Grieder, Extensive Air Showers, Springer-Verlag Berlin, Heidelberg, 2010. doi:10.1007/978-3-540-76941-5.

[4] J. Grisales-Casadiegos, C. Sarmiento-Cano, L. A. Núñez, Impact of global data assimilation system atmospheric models on astroparticle showers, Canadian Journal of Physics 100 (2022) 152–157.

[5] J. Blümer, R. Engel, J. R. Hörandel, Cosmic rays from the knee to the highest energies, Progress in Particle and Nuclear Physics 63 (2009) 293–338. doi:10.1016/j.ppnp.2009.05.002.

[6] K.-H. Kampert, A. A. Watson, Extensive air showers and ultra high-energy cosmic rays: a historical review, The European Physical Journal H 37 (2012) 359–412.

[7] P. Abreu, M. Aglietta, E. Ahn, I. F. d. M. Albuquerque, D. Allard, I. Allekotte, J. Allen, P. Allison, A. Almeda, J. A. Castillo, et al., Measurement of the proton-air cross section at $\sqrt{s} = 57\,\text{Tev}$ with the pierre auger observatory, Physical review letters 109 (2012) 062002.

[8] K. Greisen, Cosmic ray showers, Annual Review of Nuclear Science 10 (1960) 63–108. doi:10.1146/annurev.ns.10.120160.000431.

[9] P. Zyla, et al. (Particle Data Group), Review of Particle Physics, PTEP 2020 (2020) 083C01. doi:10.1093/ptep/ptaa104, and 2021 update.

[10] J. Matthews, A heitler model of extensive air showers, Astroparticle Physics 22 (2005) 387–397.

[11] C. D. Roberts, M. Bhagwat, A. Höll, S. Wright, Aspects of hadron physics, The European Physical Journal Special Topics 140 (2007) 53–116.

[12] J. Capdevielle, The influence of baryon resonances and vector mesons on cosmic ray cascades, Journal of Physics G: Nuclear and Particle Physics 18 (1992) L43.

[13] R. Silberberg, C. Tsao, Spallation processes and nuclear interaction products of cosmic rays, Physics Reports 191 (1990) 351–408.

[14] P. Goldhagen, Cosmic-ray neutrons on the ground and in the atmosphere, MRS bulletin 28 (2003) 131–135.

[15] J. Clem, G. De Angelis, P. Goldhagen, J. Wilson, New calculations of the atmospheric cosmic radiation field—results for neutron spectra, Radiation protection dosimetry 110 (2004) 423–428.

[16] I. Sidelnik, H. Asorey, et al., LAGO: The Latin American giant observatory, Nuclear Instruments and Methods in Physics Research Section A: Accelerators, Spectrometers, Detectors and Associated Equipment 876 (2017) 173–175.

[17] H. Asorey, M. Suárez-Durán, et al., The ARTI framework: Cosmic rays atmospheric background simulations, 2015. URL: https://github.com/lagoproject/arti.

[18] C. Sarmiento-Cano, M. Suárez-Durán, A. Vásquez Ramírez, A. Jaimes-Motta, R. Calderón-Ardila, J. Peña-Rodríguez, Modeling the lago's detectors response to secondary particles at ground level from the antarctic to mexico, in: Proceedings of 36th International Cosmic Ray Conference, volume PoS(ICRC2019), 2019, pp. 1–4. doi:10.22323/1.358.0412.

[19] H. Asorey, S. Dasso, L. Núñez, Y. Pérez, C. Sarmiento-Cano, M. Suárez-Durán, et al., The lago space weather program: Directional geomagnetic effects, background fluence calculations and multi-spectral data analysis, in: The 34th International Cosmic Ray Conference, volume PoS (ICRC2015), volume 142, 2015.

[20] C. Sarmiento-Cano, H. Asorey, J. Sacahui, L. Otiniano, I. Sidelnik, The latin american giant observatory (lago) capabilities for detecting gamma ray bursts, in: Proceedings of 37th International Cosmic Ray Conference, volume PoS(ICRC2021), 2021, pp. 1–4. doi:10.22323/1.395.0929.

[21] P. A. collaboration, et al., The pierre auger observatory and its upgrade, Science Reviews-from the end of the world 1 (2020) 8–33.

[22] A. Galindo, E. Moreno, E. Carrasco, I. Torres, A. Carramiñana, M. Bonilla, H. Salazar, R. Conde, W. Alvarez, C. Alvarez, et al., Calibration of a large water-cherenkov detector at the sierra negra site of lago, Nuclear Instruments and Methods in Physics Research Section A: Accelerators, Spectrometers, Detectors and Associated Equipment 861 (2017) 28–37.

[23] J. Peña-Rodríguez, L. A. Núñez, H. Asorey, Characterization of the muography background using the muon telescope (mute), in: Proceed-

ings of 40th International Conference on High Energy physics, volume PoS(ICHEP2020), 2021, pp. 1–4. doi:10.22323/1.390.0984.

[24] A. Aab, P. Abreu, M. Aglietta, J. M. Albury, I. Allekotte, A. Almela, J. A. Castillo, J. Alvarez-Muñiz, R. A. Batista, G. A. Anastasi, et al., Studies on the response of a water-cherenkov detector of the pierre auger observatory to atmospheric muons using an rpc hodoscope, Journal of Instrumentation 15 (2020) P09002.

[25] C. P. Bertolli, C. Sarmiento-Cano, H. Asorey, Estimación del flujo de muones en el laboratorio subterráneo andes, in: ANALES AFA, volume 32, 2022, pp. 106–111.

[26] J. Peña-Rodríguez, A. Vesga-Ramírez, A. Vásquez-Ramírez, M. Suárez-Durán, R. de León-Barrios, D. Sierra-Porta, R. Calderón-Ardila, J. Pisco-Guavabe, H. Asorey, J. Sanabria-Gómez, et al., Muography in colombia: simulation framework, instrumentation and data analysis, Journal for Advanced Instrumentation in Science 2022 (2022).

[27] A. Taboada, C. Sarmiento-Cano, A. Sedoski, H. Asorey, Meiga, a dedicated framework used for muography applications, Journal for Advanced Instrumentation in Science 2022 (2022). doi:10.31526/jais.2022.266.

[28] A. Vásquez-Ramírez, M. Suárez-Durán, A. Jaimes-Motta, R. Calderón-Ardila, J. Peña-Rodríguez, J. Sánchez-Villafrades, J. Sanabria-Gómez, H. Asorey, L. Núñez, Simulated response of mute, a hybrid muon telescope, Journal of Instrumentation 15 (2020) P08004.

[29] A. Vesga-Ramírez, J. Sanabria-Gómez, D. Sierra-Porta, L. Arana-Salinas, H. Asorey, V. Kudryavtsev, R. Calderón-Ardila, L. Núñez, Simulated annealing for volcano muography, Journal of South American Earth Sciences 109 (2021) 103248.

[30] A. Vásquez-Ramírez, M. Ariza-Gómez, M. Carrillo-Moreno, V. Baldovino-Medrano, H. Asorey, L. Núñez, Improvised explosive devices and cosmic rays, in: Proceedings of 37th International Cosmic Ray Conference, volume PoS(ICRC2021), 2021, pp. 1–4. doi:10.22323/1.395.0480.

[31] I. Sidelnik, H. Asorey, N. Guarín, M. S. Durán, M. G. Berisso, J. Lipovetzky, J. J. Blostein, Simulation of 500 mev neutrons by using nacl doped

water cherenkov detector, Advances in Space Research 65 (2020) 2216–2222.

[32] I. Sidelnik, H. Asorey, N. Guarin, M. S. Durán, J. Lipovetzky, L. H. Arnaldi, M. Pérez, M. S. Haro, M. G. Berisso, F. A. Bessia, et al., Enhancing neutron detection capabilities of a water cherenkov detector, Nuclear Instruments and Methods in Physics Research Section A: Accelerators, Spectrometers, Detectors and Associated Equipment 955 (2020) 163172.

[33] I. Sidelnik, H. Asorey, N. Guarin, M. S. Durán, F. A. Bessia, L. H. Arnaldi, M. G. Berisso, J. Lipovetzky, M. Pérez, M. S. Haro, et al., Neutron detection capabilities of water cherenkov detectors, Nuclear Instruments and Methods in Physics Research Section A: Accelerators, Spectrometers, Detectors and Associated Equipment 952 (2020) 161962.

[34] F. Kneizys, et al., The MODTRAN 2/3 report and LOWTRAN 7 model, Technical Report, Phillips Laboratory, Hanscom AFB, MA (USA), 1996.

[35] N. O. National Aerospace Administration (NASA), A. A. (NOAA), U. A. Force, US Standard Atmosphere 1976, NOAA technical report NOAA-S/T-76-1562, National Oceanic and Atmospheric Administration, 1976.

[36] NOAA Air Resources Laboratory (ARL), Global data assimilation system (gdas1) archive information, 2004. URL: http://ready.arl.noaa.gov/gdas1.php.